

Correlation of microstructure and magnetic softness of Si-microalloying FeNiBCuSi nanocrystalline alloy revealed by nanoindentation

Benjun Wang(汪本军), Wenjun Liu(刘文君), Li Liu(刘莉), Yu Wang(王玉), Yu Hang(杭宇), Xinyu Wang(王新宇), Mengen Shi(施蒙恩), Hanchen Feng(冯汉臣), Long Hou(侯龙), Chenchen Yuan(袁晨晨), Zhong Li(李忠), and Weihuo Li(李维火)

Citation: Chin. Phys. B, 2024, 33 (**12**): 126101. DOI: 10.1088/1674-1056/ad84c8
Journal homepage: http://cpb.iphy.ac.cn; http://iopscience.iop.org/cpb

What follows is a list of articles you may be interested in

Liquid crystal droplets formation and stabilization during phase transition process

Xia Meng(孟霞), Jiayao Ye(叶家耀), Ao Li(李澳), Xudong Zhu(朱徐栋), Zhaoyan Yang(杨朝雁), Lei Wang(王磊), Bingxiang Li(李炳祥), and Yanqing Lu(陆延青)

Chin. Phys. B, 2024, 33 (**11**): 116101. DOI: 10.1088/1674-1056/ad7afd

Pressure-induced structural, electronic, and superconducting phase transitions in $TaSe_3$

Yuhang Li(李宇航), Pei Zhou(周佩), Chi Ding(丁驰), Qing Lu(鲁清), Xiaomeng Wang(王晓梦), and Jian Sun(孙建)

Chin. Phys. B, 2024, 33 (**10**): 106102. DOI: 10.1088/1674-1056/ad6f92

Visualizing extended defects at the atomic level in a $Bi_2Sr_2CaCu_2O_{8+\delta}$ superconducting wire

Kejun Hu(胡柯钧), Shuai Wang(王帅), Boyu Li(李泊玉), Ying Liu(刘影), Binghui Ge(葛炳辉), and Dongsheng Song(宋东升)

Chin. Phys. B, 2024, 33 (**9**): 096101. DOI: 10.1088/1674-1056/ad6ccd

Geometries and electronic structures of $Zr_nCu(n=2\text{-}12)$ clusters: A joint machine-learning potential density functional theory investigation

Yizhi Wang(王一志), Xiuhua Cui(崔秀花), Jing Liu(刘静), Qun Jing(井群), Haiming Duan(段海明), and Haibin Cao(曹海宾)

Chin. Phys. B, 2024, 33 (**1**): 016109. DOI: 10.1088/1674-1056/acd5c2

Dislocation mechanism of $Ni_{47}Co_{53}$ alloy during rapid solidification

Yun-Chun Liu(刘云春), Yong-Chao Liang(梁永超), Qian Chen(陈茜), Li Zhang(张利), Jia-Jun Ma(马家君), Bei Wang(王蓓), Ting-Hong Gao(高廷红), and Quan Xie(谢泉)

Chin. Phys. B, 2023, 32 (**6**): 066104. DOI: 10.1088/1674-1056/aca7ea

---

Correlation of microstructure and magnetic softness of Si-microalloying FeNiBCuSi nanocrystalline alloy revealed by nanoindentation

Benjun Wang(汪本军)[1], Wenjun Liu(刘文君)[1], Li Liu(刘莉)[1], Yu Wang(王玉)[1], Yu Hang(杭宇)[1], Xinyu Wang(王新宇)[1], Mengen Shi(施蒙恩)[1], Hanchen Feng(冯汉臣)[3], Long Hou(侯龙)[1,2,†], Chenchen Yuan(袁晨晨)[3], Zhong Li(李忠)[4], and Weihuo Li(李维火)[1,2]

[1] *School of Materials Science and Engineering, School of Metallurgical Engineering, Anhui University of Technology, Ma'anshan* 243002, *China*
[2] *Wuhu Technology and Innovation Research Institute, Wuhu* 242000, *China*
[3] *School of Materials Science and Engineering, Instrumental Analysis Center, Southeast University, Nanjing* 211189, *China*
[4] *Institute of Advanced Magnetic Materials, College of Materials and Environmental Engineering, Hangzhou Dianzi University, Hangzhou* 310012, *China*

(Received 3 July 2024; revised manuscript received 27 September 2024; accepted manuscript online 9 October 2024)

Compared to the commercial soft-magnetic alloys, the high saturation magnetic flux density (B_s) and low coercivity (H_c) of post-developed novel nanocrystalline alloys tend to realize the miniaturization and lightweight of electronic products, thus attracting great attention. In this work, we designed a new FeNiBCuSi formulation with a novel atomic ratio, and the microstructure evolution and magnetic softness were investigated. Microstructure analysis revealed that the amount of Si prompted the differential chemical fluctuations of Cu element, favoring the different nucleation and growth processes of α-Fe nanocrystals. Furthermore, microstructural defects associated with chemical heterogeneities were unveiled using the Maxwell–Voigt model with two Kelvin units and one Maxwell unit based on creeping analysis by nanoindentation. The defect, with a long relaxation time in relaxation spectra, was more likely to induce the formation of crystal nuclei that ultimately evolved into the α-Fe nanocrystals. As a result, $Fe_{84}Ni_2B_{12.5}Cu_1Si_{0.5}$ alloy with refined uniform nanocrystalline microstructure exhibited excellent magnetic softness, including a high B_s of 1.79 T and very low H_c of 2.8 A/m. Our finding offers new insight into the influence of activated defects associated with chemical heterogeneities on the microstructures of nanocrystalline alloy with excellent magnetic softness.

Keywords: nanocrystalline alloy, magnetic softness, microstructures, defects, nanoindentation

PACS: 61.43.Dq, 65.60.+a, 75.60.Ej **DOI:** 10.1088/1674-1056/ad84c8

1. Introduction

As an important energy material, the development of soft-magnetic alloys plays a crucial role in minimizing energy dissipation. Thereinto, Fe-based amorphous/nanocrystalline alloys have attracted great interest owing to their excellent soft-magnetic properties (SMPs) such as high saturation magnetic flux density (B_s), low coercivity (H_c), high effective permeability (μ_e) and low loss (P).[1–3] Making a general survey on high-performance nanocrystalline alloys, the commercialized ones reported at present are still mainly based on FeSiBNbCu alloy, which exhibit relatively low B_s of $\sim$ 1.24 T, much lower than that of Si-steel ($\sim$ 1.97 T),[4,5] thus limiting their large-scale commercial applications. To address this critical issue, great efforts have been made through tailoring the composition, processing techniques, and heat treatment modes for stress relieving and nanocrystallization.[6–9] Hereinto, the composition fine-tuning as the main structure–property optimization strategy is employed by two paths. One is the substitution of Fe by Co element utilizing their exchange-coupling interaction,[10–12] which can give rise to high B_s but deteriorate the magnetic softness, thus requiring special heat treatment such as magnetic field annealing and ultrafast annealing.[13,14] The other one is the addition of metalloid elements (C, B, Si, and P) according to the sp–d hybridization between metal and metalloid elements.[15–17] This policy cannot greatly improve the B_s but significantly optimize the H_c, resulting in acceptable comprehensive magnetic properties, and is therefore widely performed. As we know, the Si element as a big-size atom seems to have high theoretical coordination numbers, which increases the metalloid-sp/metal-d bonding, hence resulting in the degradation of B_s in amorphous alloys as well as α-Fe nanocrystals. Interestingly, massive alloy systems are reported that have more or less Si content, revealing the necessity and importance of Si elements.[4,18,19] For instance, in the case of commercial FINEMET alloy ($Fe_{73.5}Si_{15.5}B_7Cu_1Nb_3$, $Fe_{73.5}Nb_3Si_{13.5}B_9Cu_1$),[2,20] Si cannot be removed from the FINEMET alloys as it plays a crucial role in controlling the microstructure although B_s drops with the inclusion of Si.[21–23] Therefore, it is essential to deeply investigate the influence of Si doping on microstructures and properties of Fe-based amorphous/nanocrystalline alloys.

To avoid the reduction of B_s caused by the excessive addition of metalloid elements, some works realize a magnetically soft nanostructure in melt-spun novel systems with an excep-

†Corresponding author. E-mail: longhou@ahut.edu.cn

© 2024 Chinese Physical Society and IOP Publishing Ltd

tionally low content of nonmagnetic additives (< 5 wt.%). The Cu-free $Fe_{85}B_{13}Ni_2$ nanocrystalline alloy with superb magnetic softness, including a low H_c of 4.6 A/m and a high B_s of 1.90 T, was proposed but needed a very high heating rate to control the nucleation and growth of nanocrystals.[24] The effects of Fe content and annealing temperature on the microstructure, thermal stability, and soft-magnetic properties of Fe-rich FeBCu alloys were reported.[25] The $Fe_{85}B_{13.5}Cu_{1.5}$ system exhibited a high B_s of 208 emu/g but a large H_c of 35 A/m. Moreover, the magnetic softness including B_s, H_c, and core loss of the Fe-rich FeBCu and FeBNi nanocrystalline alloys was analyzed in-depth by Parsons,[26] but it was found that excellent magnetic properties were still controlled by the ultrafast annealing process, which deviated the level of industrial production.

Motivated by these studies, to investigate the influence of minor Si addition on the structure–property of alloy and increase the possibility of industrial production, the FeB alloy with Ni and Cu adding was selected owing to the low saturation magnetostriction of Ni element[27] and the nucleation of α-Fe phase favored by Cu element.[28] Then, the effects of B substitution by minor Si on microstructure and magnetic softness of $Fe_{84}Ni_2B_{13-x}Cu_1Si_x$ alloys were investigated in detail via conventional annealing. Also, the structural heterogeneity in the amorphous matrix was analyzed by nanoindentation to reveal the structural evolution.

2. Experimental details

Master ingots with the nominal compositions of $Fe_{84}Ni_2B_{13-x}Cu_1Si_x$ ($x = 0.5$ at.%, 1 at.% and 2 at.%) were produced by high-frequency induction melting the mixtures of Fe (99.99 mass %), Ni (99.99 mass%), B (99.99 mass%), Cu (99.995 mass%) and Si (99.999 mass%) in a high-purity argon atmosphere, and then the as-quenched (AQ) ribbons with a width of $\sim$ 1 mm and a thickness of 18–22 μm were prepared by a single roller melt-spinning method in an argon atmosphere. Here, the linear speed of the copper wheel was set to 45 m/s and the injection pressure was maintained at $\sim$ 0.02 MPa. Similar to our previous works,[29] the AQ ribbons were isothermally annealed to develop nanocrystalline alloys. The annealing was performed by keeping the ribbons in a quartz tube under vacuum atmosphere (10^{-3} Pa), and then pushing the quartz tube into a tubular furnace preheated to annealing temperature (360–460 °C) for various times followed by water quenching cooling.

Microstructures were examined by x-ray diffraction (XRD, Bruker D8 Discover) with Cu $K\alpha$ radiation and transmission electron microscopy (TEM, Talos F200X) equipped with an EDS detector. Thermal behaviors were measured by using a differential scanning calorimeter (DSC, NETZSCH 449 F3) under a flow of high-purity argon with a heating rate of 0.67 °C/s. Magnetic properties including B_s and H_c were measured using a vibrating sample magnetometer (VSM, MicroSense-EZ7) under a maximum applied field of 800 kA/m and a B–H loop tracer (RIKEN BHS-40) under a maximum applied field of 1 kA/m. Mechanical properties were evaluated by nanoindentation (NanoIndenter G200) at room temperature with a standard Berkovich diamond indenter. The tests were carried out at a maximum load of 50 mN under loading and unloading rate of 5 mN/s followed by a holding period of 30 s at peak load. Here, to minimize the random error, we set up a 10 by 10 rectangular area with a total of 100 points for nanoindentation tests. The related data points with errors exceeding the preset threshold were excluded, and then the effective data were statistically analyzed in this work.

3. Results and discussion

Figure 1 shows the microstructures and thermal behaviors of the AQ $Fe_{84}Ni_2B_{13-x}Cu_1Si_x$ ($x = 0.5$ at.%, 1 at.% and 2 at.%) alloys. As shown in Fig. 1(a), within the distinguishable range of XRD, only a halo peak near 45° on the pattern without obvious sharp diffraction peaks of crystallization for each alloy is detected, unveiling a fully amorphous structure. Thermal parameters of the AQ alloys were measured with results shown in Fig. 1(b). All curves exhibit two distinctly separated exothermic peaks, corresponding to the two stages of the crystallization process. The first and second onset crystallization temperatures, marked as T_{x1} and T_{x2} in the figure, are related to the precipitation of α-Fe and compound phases

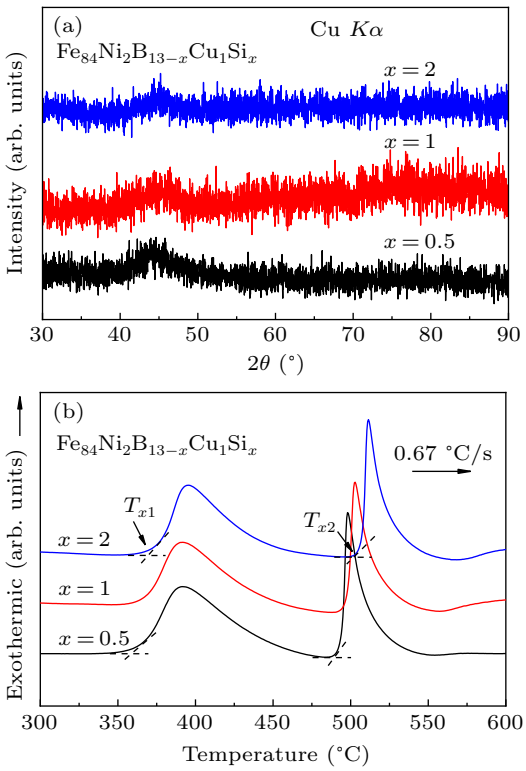


Fig. 1. (a) XRD patterns and (b) DSC curves of AQ $Fe_{84}Ni_2B_{13-x}Cu_1Si_x$ ($x = 0.5$ at.%, 1 at.% and 2 at.%) amorphous alloys.

from the amorphous matrix.[10,28] This is the typical thermodynamic characteristic of amorphous alloys and matches well with the XRD results. Besides, both T_{x1} and T_{x2} slightly move to a high temperature with Si increasing, and then a larger crystallization window ΔT $(= T_{x2} - T_{x1})$ of 131 °C can be obtained at 2 at.% Si addition. This result consists well with that reported in FeCuSiB alloys,[21] revealing an enhanced thermal stability of the residual amorphous phase by the addition of Si.

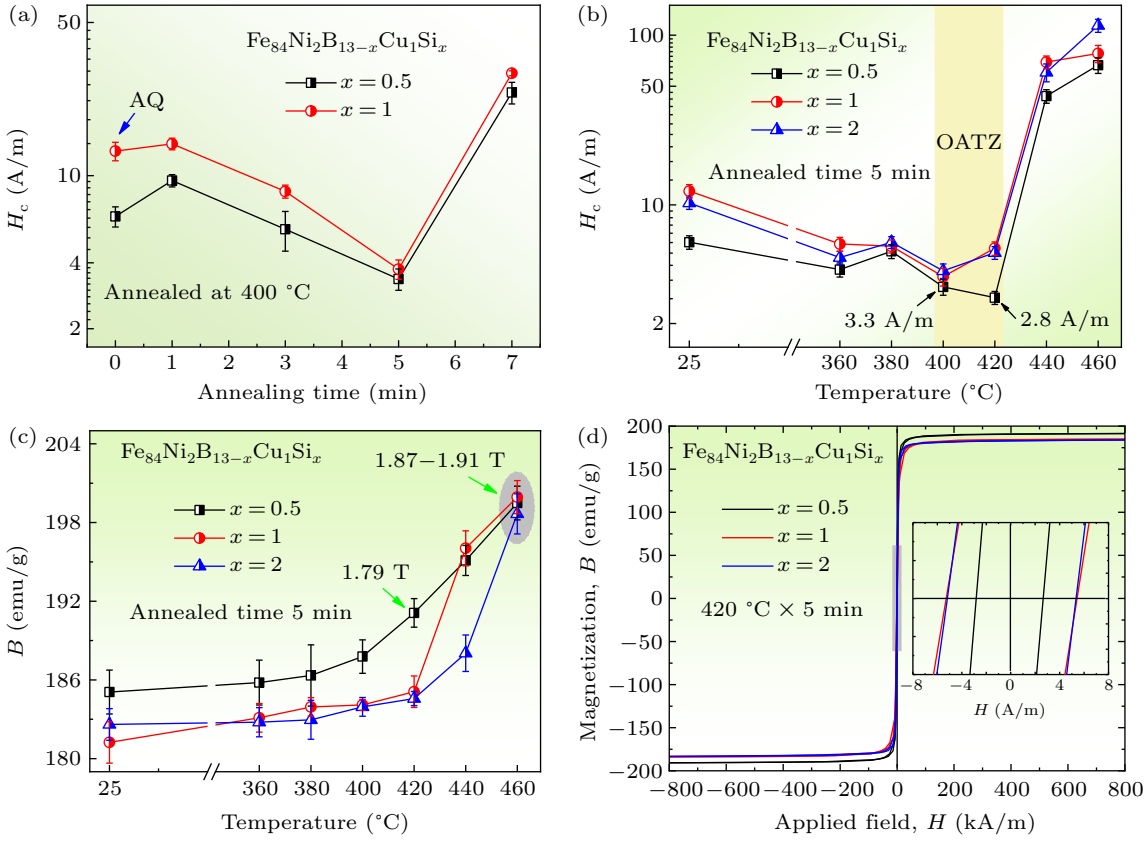


Fig. 2. Magnetization performance of FeNiBCuSi alloys during the annealing process.

The magnetic properties of the AQ $Fe_{84}Ni_2B_{13-x}Cu_1Si_x$ alloys were investigated in detail as shown in Fig. 2. To confirm the reasonable annealing time (t_a), the alloys with 0.5 at.% and 1 at.% Si addition were selected and annealed at 400 °C, which is in the vicinity of the first crystallization peak on each DSC curve to ensure the crystallization. As displayed in Fig. 2(a), a similar tendency of the H_c changes dependence on t_a for both alloys is observed, which firstly drops and then increases. The minimum of H_c of 3.3 A/m is obtained for 0.5 at.% Si-added alloy annealed at 400 °C for 5 min, confirming a better t_a. Figure 2(b) shows the dependence of H_c on annealing temperature (T_a) for $Fe_{84}Ni_2B_{13-x}Cu_1Si_x$ alloys. All alloys exhibit the same variation tendency with T_a changing, i.e., the H_c undergoes a typical W-like process (decrease–increase–decrease–increase) followed by a distinct rise at 460 °C. The first decline of H_c can be easily caused by more efficient stress relief and uniformity of structure enhanced by structural relaxation, but the increase at 380 °C may be attributed to the precipitation of a small amount of α-Fe crystals, which can trigger a large uniaxial magnetocrystalline anisotropy constant of the amorphous system. As T_a is near or higher than T_{x2}, the rapid growth of α-Fe grains and the precipitation of non-ferromagnetic compounds (Fe–B) will greatly degrade the soft-magnetic properties.[10,11] That is the reason for the largest H_c at 460 °C. It is well known that annealing temperature between T_{x1} and T_{x2} will induce the high density of α-Fe nanograins dispersed in the amorphous matrix, which is expected to favor the improvement of soft-magnetic properties. As a result, the optimum annealing temperature zone (OATZ) of 400–420 °C for current alloys can be confirmed. Related to the H_c changes, the T_a dependence of B_s of the FeNiBCuSi alloys is exhibited in Fig. 2(c). The B_s decreases firstly and then increases slightly for the AQ alloy with Si added, which may be attributed to the strong pd hybridization between Fe and B/Si elements.[16,17] As T_a increases, a gradually increasing process on B_s with the large value of 1.87–1.91 T at 460 °C can be affirmed, presenting a high application potential if the H_c is further optimized. Interestingly, the 0.5 at.% Si-added alloy seems to show a larger B_s compared to that with 1 at.% and 2 at.% Si addition under the same conditions. Especially at 420 °C, the excellent comprehensive magnetic properties with large B_s of 1.79 T and very

low H_c of 2.8 A/m are achieved. Subsequently, the comparison of the hysteresis loops of FeNiBCuSi alloys annealed at 420 °C for 5 min is shown in Fig. 2(d). There is a typical rectangular loop for each case, where the magnetization quickly saturates at a low applied field, suggesting a good magnetic response. The detailed H_c in the vicinity of the zero field is shown in the inset. The alloy with 0.5 at.% Si addition exhibits low $H_c < 3.0$ A/m, meanwhile, a large slope can also be found for the current alloy, indicating a high permeability at an applied field of 1 kA/m.

To elucidate the underlying mechanism of magnetic softness, the microstructure of 0.5 at.% Si-added alloy was first investigated via TEM, as shown in Fig. 3. One can see from Fig. 3(a) that the composite structure consisting of some grains and visibly residual amorphous matrix can be discerned after annealing at 400 °C. Similar to the previous works,[30,31] the selected area electron diffraction (SAED) pattern in the inset further verifies the precipitation of α-Fe nanograins in the matrix. The detailed grain distribution obtained by analysis software (Nano Measurer 1.2) is shown in Fig. 3(b). Statistic result reveals that the grain size (D) mainly distributes from 15 nm to 55 nm with 30 nm on average. The lower density of the grains leads to a weakened competitive growth between the nanocrystals, combined with the absence of diffusion-suppression, resulting in the slight crystals coarsening. Inversely, the massive precipitated nanocrystals, which were further verified to be the single α-Fe phase, are observed for the alloy after annealing at 420 °C (Fig. 3(c)). Note that the average D revealed by grain statistics in Fig. 3(d) is $\sim$ 20.3 nm, much smaller than that at 400 °C, unveiling a process of grain refinement as the T_a properly increases. Moreover, compared to that in Fig. 3(b), there exist some small grains with D below 15 nm embedded in the amorphous matrix, revealing the coupled growth of α-Fe nanocrystals accompanied by the nucleation and growth of small grains.

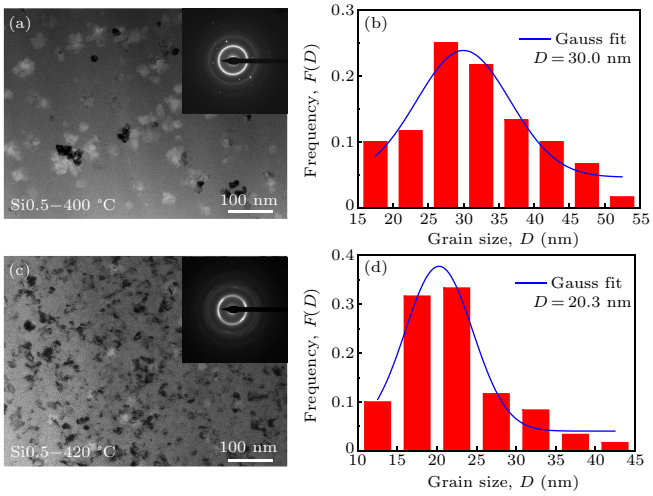


Fig. 3. Microstructures of annealed $Fe_{84}Ni_2B_{12.5}Cu_1Si_{0.5}$ alloys: [(a) and (c)] bright-field TEM images, and [(b) and (d)] corresponding grain size distributions.

As we know, for the alloy after crystallization, the B_s can be comprehended from the crystallization volume fraction (V_{cry}) of α-Fe nanocrystals, and determined by the following equation:[32,33]

$$B_s = B_{sc}V_{cry} + B_{sa}(1 - V_{cry}), \tag{1}$$

where B_{sc} of 2.1 T and B_{sa} of 1.5 T are the saturation magnetization of α-Fe crystalline and amorphous phases, respectively. Distinctly, the enhanced B_s is mainly attributed to the increasing V_{cry} of α-Fe nanocrystals once the alloy occurs crystallization. In addition to the XRD and Mossbauer spectroscopy, the V_{cry} can also be widely calculated based on the DSC curves according to the following equation:[34,35]

$$V_{cry} = 1 - \Delta H_o'/\Delta H_o, \tag{2}$$

where ΔH_o and $\Delta H_o'$ are the heat releases of crystallization for the as-spun and the annealed samples, respectively. As a result, the DSC curves of the alloy before and after annealing are shown in Fig. 4. The obvious diversities for all curves can be found, in which the intensity of the first crystalline diffraction peak gradually drops while the other one is almost unchanged with T_a increasing. It implies that the precipitation of the α-Fe phase from the amorphous matrix has happened without non-ferromagnetic compounds, which matches well with the TEM results. The V_{cry} calculated by Eq. (2) is 24.2% for 400 °C and 45.5% for 420 °C. Combined with the grain size from Figs. 3(b) and 3(d), it can be inferred that the higher V_{cry} and lower D of the alloy annealed at 420 °C favor a large B_s. The low H_c for nanocrystalline alloys can be understood based on Herzer's effective magnetic random anisotropy model,[36] in which the H_c can be discussed by the following equation:

$$H_c = P_c\frac{\langle K\rangle}{J_s}, \tag{3}$$

where P_c is the dimensionless pre-factor of the order of unity, and J_s is the average saturation polarization of the material. Then, $\langle K\rangle$ is further analyzed by the random magnetocrystalline anisotropy $\langle K_1\rangle$, induced uniaxial anisotropies K_u, and magnetoelastic anisotropy K_μ^{el}.[9,36] The K_u is closely associated with the existence of magnetic atomic pair ordering in alloy systems and can be determined by magnetic field annealing,[37] whereas the K_μ^{el} is affected by the internal stress (σ) and saturation magnetostriction coefficient (λ_s).[38] In a dual-phase structure, the K_u is relatively small and thus should be negligible under normal annealing. With the precipitation of α-Fe, the K_μ^{el} decreases gradually due to the drop of the λ_s. Thus, the $\langle K\rangle$ is mainly determined by the $\langle K_1\rangle$, which can be described as[36]

$$\langle K_1\rangle = \frac{K_1}{\sqrt{N}} = K_1 \times (D/L_{ex})^{3/2}, \tag{4}$$

where K_1 and N are the local magneto-crystalline anisotropy and the number of α-Fe nanograins in a magnetically coupled volume, respectively. Obviously, when the D is smaller

than the exchange–correlation length ($L_{ex} \approx 40$ nm[39]), the decreased $\langle K_1 \rangle$ caused by the strong exchange-coupling between crystallites triggers a low H_c. That is why the alloy after annealing 420 °C exhibits the lowest H_c of 2.8 A/m.

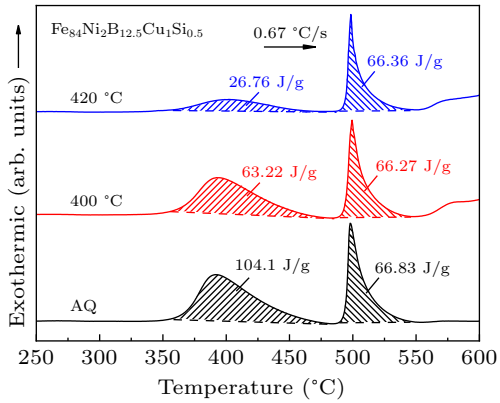


Fig. 4. Analysis of the ΔH in the first and second exothermic peaks of the FeNiBCuSi alloy before and after annealing.

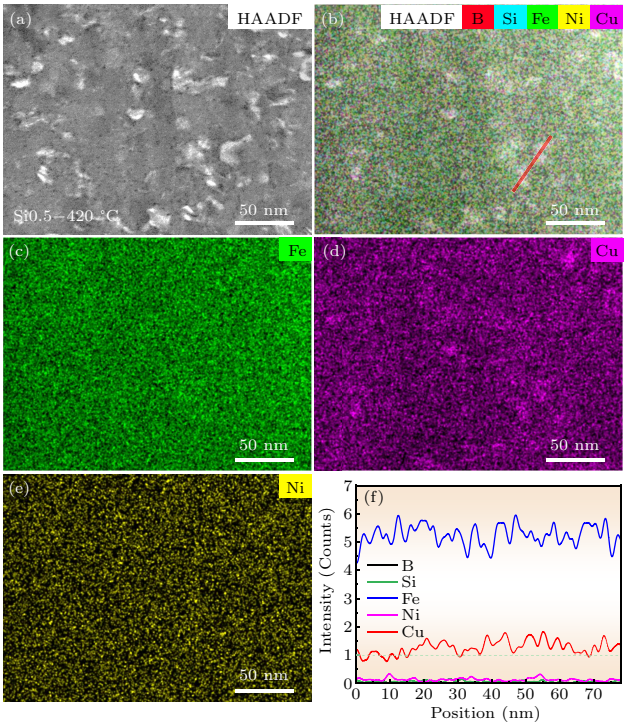


Fig. 5. High-angle annular dark field (HAADF) images and related elemental mappings of the $Fe_{84}Ni_2B_{12.5}Cu_1Si_{0.5}$ alloy after annealing at 420 °C for 5 min: (a) HAADF; (b) 2D element distribution mapping; (c)–(e) Fe, Cu, and Ni mappings; (f) atomic concentration depth profile from a randomly selected region of two adjacent grains in (b).

Next, to further explore the influence of possible nanoscale chemical fluctuations on nucleation and growth of α-Fe nanograins, the high-resolution Z-contrast high-angle annular dark field scanning transmission electron microscope (HAADF-STEM) analysis for 0.5 at.% Si-added alloy was carried out with results shown in Fig. 5. As can be seen, a distinct dark-bright substrate in Fig. 5(a) can be observed. According to the TEM result in Fig. 3(c), this contrast is attributed to the precipitation of α-Fe grains in the amorphous matrix instead of the inhomogeneous distribution of density reported by Luo.[14] The structural heterogeneity of the matrix is expounded by the STEM mapping of elements in Fig. 5(b), where it is revealed via the white areas different from the matrix. The evident difference in element distribution between Fe, Ni, and Cu can be seen in Figs. 5(c)–5(e). Here B and Si elements are not given owing to the small size and light of the former, and the low content of the latter. The Fe and Ni elements showing no chemical fluctuations may reveal the similar respective Fe and Ni contents in the amorphous matrix and the nanocrystals. In contrast, the Cu element undergoes apparent chemical segregation, defined as the Cu-rich and Cu-poor regions. Although no fluctuation of Fe element is detected, the Cu clusters serve as the heterogeneous nucleation sites for the formation of the refined α-Fe nanocrystals,[40] revealing the subsequent precipitation mechanism of the α-Fe phase. This result is further clarified by the concentration depth profiles (Fig. 5(f)). The Fe element exhibits a homogeneous atomic spatial fluctuation but a slight rise in Cu element in nanograins instead, disclosing the importance of Cu in the formation of nanocrystals.

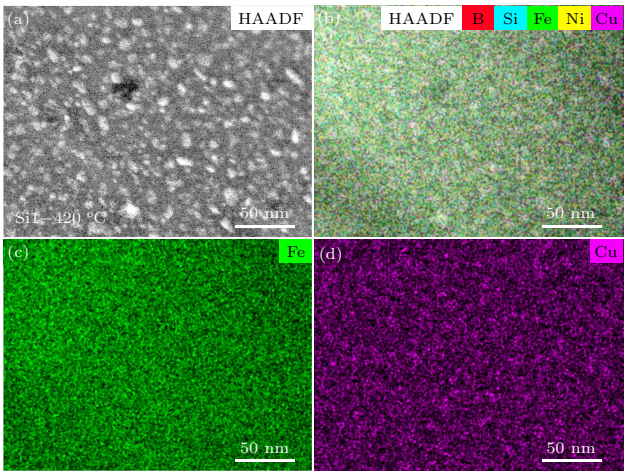


Fig. 6. Microstructure of $Fe_{84}Ni_2B_{12}Cu_1Si_1$ alloy after annealing at 420 °C for 5 min with (a) HAADF image; (b) 2D element distribution mapping; (c)–(d) Fe and Cu mappings.

The microstructure of the alloy with 1 at.% Si added was also investigated via HAADF-STEM for comparison, as shown in Fig. 6. Compared to Fig. 5(a), a distinct contrast exists in Fig. 6(a), where a large number of nanograins in the matrix are substituted by massive cluster-like areas with diameters below 10 nm. The STEM mappings exhibit a relatively homogeneous distribution in Fig. 6(b). Visible correlation between chemical segregation and heterogeneity (Fig. 6(c)) cannot be detected, similar to the structure of 0.5 at.% Si-added alloy. Interestingly, the remarkable keel-like Cu fluctuations are observed in Fig. 6(d). It can be inferred from Fig. 2(d) that the low B_s of the present alloy means less precipitated α-Fe phase with low V_{cry}. That is to say, before α-Fe nanograins

nucleation, even if massive Cu clusters precipitate, the magnetization of the alloy is still mainly determined by the amorphous matrix, as revealed in FeNiBCu alloy system that the increase in the density of Fe clusters does not significantly enhance the B_s.[27]

The early works have demonstrated that the plastic deformation during the creep originating from the anelastic and viscoplastic behaviors is closely associated with the microstructural heterogeneity (defect) in the amorphous matrix.[14,41] To explore the structural defects and their correlation with chemical fluctuations in the matrix, the mechanical behavior of 0.5 at.% Si-added alloy was investigated by nanoindentation. All alloys exhibit the typical load–displacement curves, which represent the three stages of loading, holding, and unloading (Fig. 7(a)). The detailed indentation information is shown in Fig. 7(b). As seen, the maximum indentation depth (h_{in}, the sum depth of the loading and holding stages) is obtained at the AQ state. The h_{in} as well as the residual depth gradually drops with T_a rising, manifesting a hardening process. Inversely, the hardness and reduced modulus gradually increase, respectively. This indicates that the atoms can cooperatively rearrange and are packed more efficiently, resulting in the degeneration of the heterogeneity and thereby the higher modulus and hardness. It suggests an enhanced ability to resist deformation. Figure 7(c) gives the holding time dependence of the creep displacement of the alloys. The creep process for each case undergoes the three stages of rapid, moderate, and steady, as presented in other Fe- and U-based alloys.[42,43] This is connected to a physical process that the defects accumulated during the loading segment will be released quickly at the beginning of the holding stage, and slowly then, and disappear eventually.[43] Consequently, the microstructure evolves accompanied by the stress relief of the residual amorphous matrix. The annihilation and reactivation of defects as well as the precipitation of α-Fe nanograins result in the decline of the creep displacement, exhibiting a hardening behavior. To further comprehend the creeping process, the Maxwell–Voigt model containing two Kelvin units and one Maxwell unit is performed to analyze the creep curves, which is commonly used for describing the creep of polymers but can also be applied to metal alloys.[41,44] As a result, the creep displacement can be described by

$$h = h_1\left(1 - e^{-t/\tau_1}\right) + h_2\left(1 - e^{-t/\tau_2}\right) + t/\mu_0, \tag{5}$$

where h_i is the indentation depth, τ_i the characteristic relaxation time for the activation of the i-th anelastic Kelvin unit, t the holding time, and μ_0 a constant of the Maxwell dashpot, which is proportional to the viscosity coefficient. Obviously, the τ_i represents the characteristic time of the different types of activated defects in the amorphous matrix, which has also been revealed by the Positron annihilation spectroscopy where the two different components for the positron lifetime are assigned

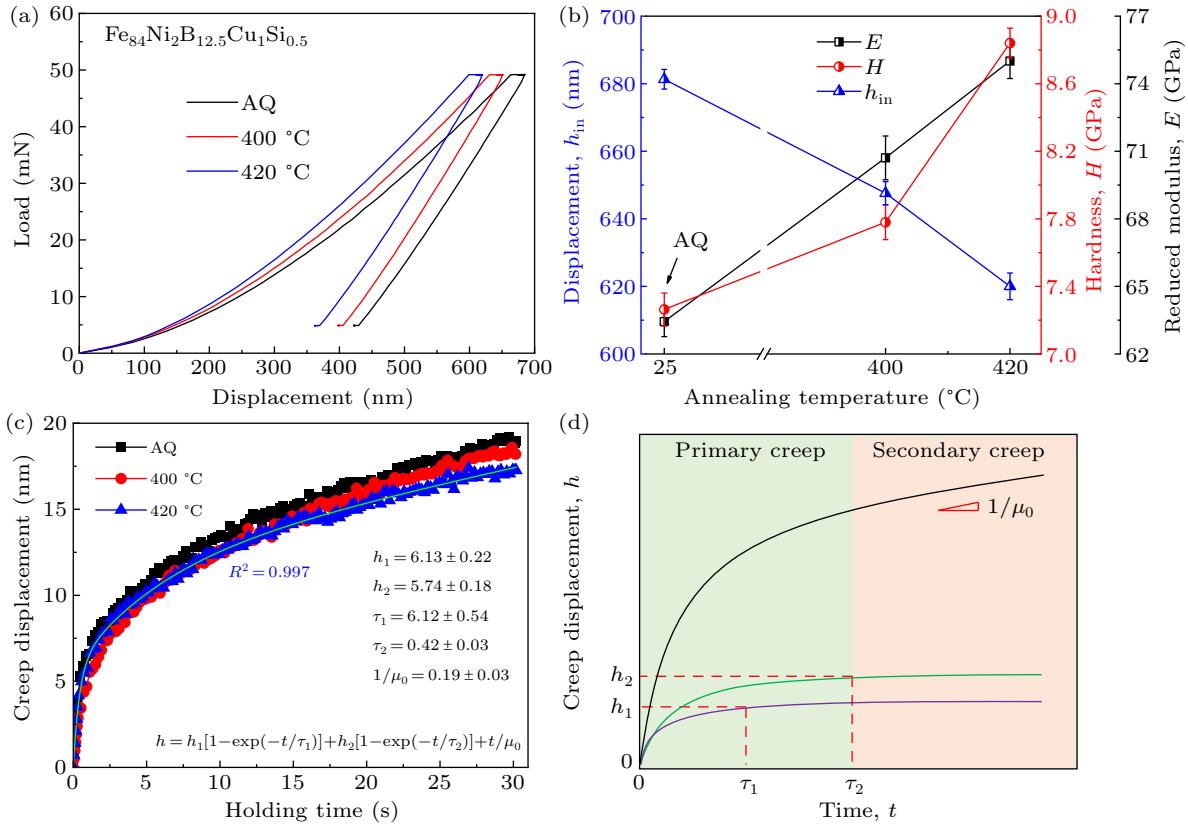


Fig. 7. Nanoindentation results of $Fe_{84}Ni_2B_{12.5}Cu_1Si_{0.5}$ alloy under the different states: (a) load–displacement curves; (b) mechanical parameters; (c) creep displacement dependence on holding time; (d) schematic diagram of the creeping process.

to the small and large defects.[41] Subsequently, the creep curve of the alloy after annealing at 420 °C is selected as an example for illustration, as shown in the fitting results in Fig. 7(c). The curve is fitted successfully by controlling the correlation coefficient R^2 to be 0.997 using Eq. (5). It further verifies that the creeping process can be assigned to the primary elastic and secondary viscous components, as shown in the schematic diagram in Fig. 7(d). The former relates to a fast but decreasing strain rate, in which the two Kelvin units reflected by changes in h_i and τ_i play a key role in the elastic behavior, while for the latter, a slow but constant strain rate μ_0^{-1} related to the one Maxwell unit can be confirmed. This result agrees well with that analyzed in Ref. [42].

The anelastic component of the creep process can be discussed in terms of a relaxation time spectrum, which supplies more details of the defect activation in the amorphous matrix during creeping, and then can be described as follows:[41,43]

$$L(\tau) = \left[\sum_{i=1}^{n}\left(1+\frac{t}{\tau_i}\right)\frac{h_i}{\tau_i}\,\mathrm{e}^{-t/\tau_i}\right]\frac{A_0}{P_0 h_{\mathrm{in}}}\,t|_{t=2\tau}\,, \tag{6}$$

where L is the spectrum intensity, A_0/P_0 the inverse of the hardness, and the parameters of h_{in}, h_i, τ, and t have been defined according to Eq. (5). Figure 8 shows the relaxation spectra of the alloy obtained at a loading rate of 5 mN/s. Two separated relaxation peaks can be observed for each case, as indicated by dynamic mechanical analysis in rare-earth- and/or Zr-, Cu-, and some Fe-based alloys that may be assigned to the β relaxation and α relaxation.[45–47] Beyond the crystallization component, the structure evolution of the residual amorphous matrix can be characterized by the relaxation time spectrum under nanoindentation. Generally, the microstructure of amorphous alloy is heterogeneous at the nanoscale, that is "defects", consisting of the loosely packed zones with large free volume (LPZs, also called liquid-like regions) and densely packed zones with small interatomic distance (DPZs).[45–48] According to the core–shell model,[43] the defects in LPZs can be broadly divided into two types: the small one corresponds to the first peak of relaxation spectra that contains few atoms and thus needs a shorter inherent relaxation time (τ_1), while the big one assigns to the second maximum consisting of more and requiring a longer time (τ_2). As a result, one can visibly see that the accepted fluctuation scale of the intensity and τ_1 of the first peak indicate a more difficult diffusion and rearrangement of atoms. This results in a difficult activation of small defects in LPZs. Whereas the intensity of the second one gradually drops and the τ_2 firstly increases and then declines. The number of activated defects drops with increasing temperature, but their sizes coupling grow, unveiling a greater sensitivity of the latter to temperature. The significant change of the characteristic relaxation time coincides with the structural heterogeneity ranging from several angstroms to dozens of nanometers found in Cu-doped FeCo-based MGs.[42] Furthermore, with the help of the atomic reconstruction schematics (Fig. 9), the microstructure evolution is analyzed. Here, the defect sites are represented by the circle areas containing some atoms, and the elastic matrix is formed by the remaining densely packed atoms. For the AQ alloy, there exist two types of defects with different sizes and numbers in the amorphous matrix, revealing the existence of heterogeneous atomic configurations at different length scales. After being annealed at 400 °C, the right-shift of the big peak reveals the coupling and reconstruction process of defects which finally glues together into a large size. It means a decrease in the density of initial large defects in LPZs, as shown in Fig. 9(b), matching well with the drop in intensity. The formation of chemically ordered structures in amorphous substrates is closely related to the cooperative diffusion and reconstruction of atoms in LPZs. In the present Si-added Fe-based amorphous alloys, the heats of mixing of Fe–Si, Ni–Si, and Cu–Si bonds are negative, being −35 kJ/mol, −40 kJ/mol, and −19 kJ/mol, respectively, which are higher than those of Fe–B, Ni–B, and Cu–B bonds.[49] In the meantime, the Cu has a large positive heat of mixing with Fe (+13 kJ/mol),[49] Fe atoms are rejected from Cu clusters and would pileup at the Cu/amorphous interface.[40] This suggests that the preferential formation of structural heterogeneity may come from the Cu-rich/ Cu-poor clusters, which is in accordance with the TEM analysis from Fig. 5(d). The heterogeneous nucleation at the Cu/amorphous interface is chemically more favorable than the homogeneous nucleation from the amorphous phase, and the fcc-Cu (111) and bcc α-Fe (110) have very good matching,[40] thus, the α-Fe will nucleate on the fcc-Cu surface with a low interfacial energy. It is noticed that as the nucleation of α-Fe with minor Si addition, the B element is forced to remain in the amorphous matrix owing to the immiscibility with Fe, which enhances the thermal stability of the residual amorphous phases, matching well with the DSC changes. During annealing, the lower temperature is not sufficient to favor the formation of chemical heterogeneities, so the heterogeneity is still mapped in terms of large-sized defects coupled to each other, as shown in Fig. 9(b). That is to say, an existing defect may grow or reconfigure itself, or a new defect may be generated as long as the elastic DPZs still remain interconnected. Thus, the fewer nucleation sites of α-Fe nanograins or Cu clusters result in the unilateral growth of α-Fe with lower density, coinciding with the Fig. 3(a) result. In contrast, the left-shift and intensity decline of the peak for the alloy annealed at 420 °C indicate a reduction in the number and size of the activated defects (Fig. 9(c)). This reveals that some LPZs evolve into localized chemically ordered structures, like clusters, since the Cu atoms are more mobile and diffuse more readily due to the repulsion of Fe–Cu, resulting in the atomic rearrangement. The α-Fe

nanograins are precipitated attaching to and enveloping these chemical heterogeneities so that the refined uniform nanocrystalline microstructure with a high density of α-Fe is formed. Meanwhile, some defects with small size and density can also be reinduced in the amorphous matrix, as depicted in Fig. 9(d). This may elucidate a clear correlation between activated defects and nanocrystalline microstructure.

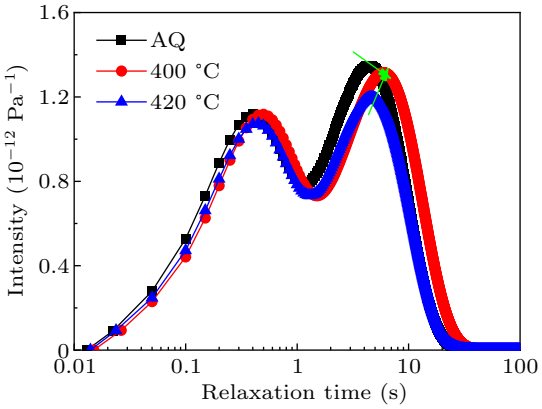


Fig. 8. Relaxation time spectra of the $Fe_{84}Ni_2B_{12.5}Cu_1Si_{0.5}$ alloy based on the anelastic part of their creep curves.

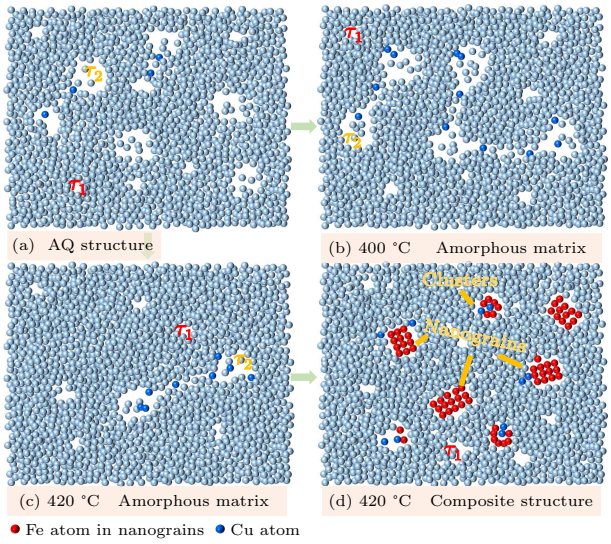


Fig. 9. Schematic diagram of atomic structure of $Fe_{84}Ni_2B_{12.5}Cu_1Si_{0.5}$ alloy: (a)–(c) amorphous/residual amorphous matrix, (d) composite structure including nanocrystalline and residual amorphous components.

Finally, we summarized the changes of B_s and H_c for current alloys and some other typical amorphous/nanocrystalline alloys for comparison, as shown in Fig. 10. It is generally accepted that an improvement in B_s is usually accompanied by an increase in H_c, presenting a trade-off relationship, especially for the Co-doped amorphous, Fe–Ni and Fe–Si nanocrystalline alloys. Here, the designed FeNiBCuSi alloy without Co element annealed at 420 °C manifests not the highest B_s but the much lower H_c instead compared to the high Fe content alloys. Anyway, it is much larger than that of the commercial FINEMET-type alloys, showing excellent comprehensive magnetic properties. This result seems to alleviate the B_s–H_c trade-off relationship.

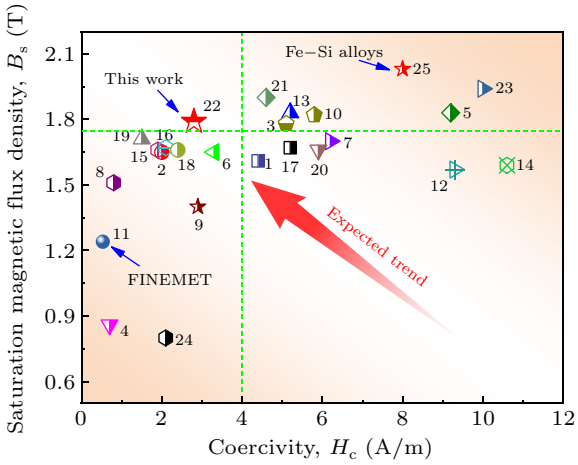


Fig. 10. Correlation of the B_s and H_c for the present alloys and twenty-four other amorphous/nanocrystalline alloys without Co element addition: 1. $Fe_{83}Si_2B_{11}P_3C_1$,[50] 2. $Fe_{83}B_{11}P_3Si_2C_1$,[51] 3. $Fe_{83}Si_3B_{11}P_2Cu_1$,[52] 4. $Fe_{38}Ni_{38}B_{12}P_5Si_3Nb_3Cu_1$,[53] 5. $Fe_{83}Ni_2B_{14}Cu_1$,[27] 6, 7. $Fe_{81}B_{10}Si_{5.5}P_{3.5}$ and $Fe_{84}B_{8.5}Si_{4.5}P_3$,[54] 8, 9. $Fe_{76}Si_9B_{10}P_5$ and $(Fe_{0.75}Si_{0.1}B_{0.15})_{96}Nb_4$,[55] 10. $Fe_{85}Si_2B_8P_4Cu_1$,[4] 11. $Fe_{73.5}Nb_3Cu_1Si_{13.5}B_9$,[20] 12. $Fe_{85}Si_{1.4}B_9Cu_{0.5}P_4C_{0.1}$,[56] 13, 14. $Fe_{83.2}P_{10}C_6Cu_{0.8}$ and $Fe_{83.2}P_8B_2C_6Cu_{0.8}$,[16] 15, 16. $Fe_{83}B_{12}Si_2P_3$ and $Fe_{83}B_{11}Si_2P_3C_1$,[57] 17–20. $Fe_{83}B_{13}Si_3P_1$, $Fe_{83}B_{11}C_2Si_3P_1$, $Fe_{83}B_{10}C_3Si_3P_1$ and $Fe_{83}B_9C_4Si_3P_1$,[15] 20. $Fe_{83.3}B_9P_3Cu_{0.7}C_4$,[15] 21. $Fe_{85}B_{13}Ni_2$,[24] 22. $Fe_{84}Ni_2B_{12.5}Cu_1Si_{0.5}$ (this work), 23. $Fe_{84.3}Si_4B_8P_3Cu_{0.7}$,[58] 24. permalloy,[59] 25. Fe–Si alloys.[59]

4. Conclusion

In this work, the effects of B substitution by minor Si on microstructure and magnetic softness of $Fe_{84}Ni_2B_{13-x}Cu_1Si_x$ alloys were investigated. The addition of 2 at.% Si expanded the crystallization window, enhancing the thermal stability of the residual amorphous matrix. Conversely, minor Si addition (0.5 at.%) had a distinctly positive effect on the magnetic softness. From the element mappings, the differential chemical fluctuations of Cu element for annealed alloys with various Si contents revealed the different nucleation and growth processes of α-Fe nanocrystals, matching well with the TEM images and grain size distributions. With the help of the nanoindentation, the creep curves related to the structural heterogeneity were fitted successfully using the Maxwell–Voigt model with two Kelvin units and one Maxwell unit. The two types of activated defects were unveiled, and the larger defect seemed to be more sensitive to the temperature, which correlated with the formation of the Cu-clusters, affording the precipitation of the α-Fe nanograins. As a result, the excellent magnetic softness of the $Fe_{84}Ni_2B_{12.5}Cu_1Si_{0.5}$ alloy after annealing at 420 °C for 5 min was obtained, which exhibited the high B_s of 1.79 T and very low H_c of 2.8 A/m.

Acknowledgments

Project supported by the Anhui Provincial Natural Science Foundation (Grant No. 2208085QE121), the Key Research & Development Plan of Anhui Province (Grant No. 2022a05020016), the University Natural Science Re-

search Project of Anhui Province (Grant No. 2023AH051084), and the National Natural Science Foundation of China (Grant No. 52071078).

References

[1] Bottauscio O 2013 *Selected Papers from the 21st Soft Magnetic Materials Conference* (SMM 21), September 1–4, 2013, Budapest, Hungary
[2] Jiang M F, Cai M J, Zhou J, Di S Y, Li X S, Luo Q and Shen B L 2023 *Mater. Today Nano* **22** 100307
[3] Zhou J, Li X S, Hou X B, Ke H B, Fan X D, Luan J H, Peng H L, Zeng Q S, Lou H B, Wang J G, Liu C T, Shen B L, Sun B A, Wang W H and Bai H Y 2023 *Adv. Mater.* **35** e2304490
[4] Makino A, Kubota T, Yubuta K, Inoue A, Urata A, Matsumoto H and Yoshida S J 2011 *Appl. Phys.* **109**
[5] Yao K F, Shi L X, Chen S Q, Shao Y, Chen N and Jia J L 2018 *Acta. Phys. Sin.* **67** 016101 (in Chinese)
[6] Stückler M, Wurster S, Weissitsch L, Krenn H, Pippan R and Bachmaier A 2021 *J. Mater. Res. Technol.* **12** 1235
[7] Stückler M, Wurster S, Pippan R and Bachmaier A 2021 *AIP Adv.* **11** 015033
[8] Li X S, Zhou J, Shen L Q, Sun B A, Bai H Y and Wang W H 2022 *Adv. Mater.* **35** 2205863
[9] Hou L, Wang B J, Liu L, Mao X H, Zhang M Y, Yuan C C, Li Z, Ju W W, Feng H C, Tang C Y, Xia A L and Li W H J 2024 *Mater. Sci. Technol.* **200** 27
[10] Hou L, Li M R, Jiang C, Fan X D, Luo Q, Chen S S, Song P D and Li W H 2021 *J. Alloys Compd.* **853** 157071
[11] Hou L, Fan X D, Wang Q Q, Yang W M and Shen B L 2019 *J. Mater. Sci. Technol.* **35** 1655
[12] Wan Q Y, Tian B, Zhang P L, Wang J H and Hua Z 2023 *Chin. Phys. B* **32** 088102
[13] Zhao C L, Wang A D, Yue S Q, Liu T, He A N, Chang C T, Wang X M and Liu C T 2018 *J. Alloys Compd.* **742** 220
[14] Luo Q, Li D H, Cai M J, Di S Y, Zhang Z G, Zeng Q S, Wang Q Q and Shen B L 2022 *J. Mater. Sci. Technol.* **116** 72
[15] Shi L X, Qin X L and Yao K F 2020 *Prog. Nat. Sci.* **30** 208
[16] Hou L, Yang W M, Luo Q, Fan X D, Liu H S and Shen B L 2020 *J. Non-Cryst. Solids* **530** 119800
[17] Sun J, Shen P F, Shang Q Z, Zhang P Y, Liu L, Li M R, Hou L and Li W H 2023 *Acta. Phys. Sin.* **72** 026101 (in Chinese)
[18] Shen B L, Inoue A and Chang C T 2004 *Appl. Phys. Lett.* **85** 4911
[19] Wang C X, Wu Z Y, Feng X M, Li Z, Gu Y, Zhang Y, Tan X H and Xu H 2020 *Intermetallics* **118** 106689
[20] Yoshizawa Y, Oguma S and Yamauchi K 1988 *J. Appl. Phys.* **64** 6044
[21] Chen Y M, Ohkubo T, Ohta M, Yoshizawa Y and Hono K 2009 *Acta Mater.* **57** 4463
[22] Parsons R, Garitaonandia J S, Yanai T, Onodera K, Kishimoto H, Kato A and Suzuki K 2017 *J. Alloys Compd.* **695** 3156
[23] Wang Y C, Zhang Y, Makino A and Kawazoe Y 2018 *J. Alloys Compd.* **730** 196
[24] Suzuki K, Parsons R, Zang B, Onodera K, Kishimoto H and Kato A 2017 *Appl. Phys. Lett.* **110** 012407
[25] Zheng Z G, Chen Y B, Wei J, Wang X, Qiu Z G and Zeng D C 2023 *J. Alloys Compd.* **939** 168621
[26] Parsons R, Zang B, Onodera K, Kishimoto H, Shoji T, Kato A and Suzuki K 2018 *J. Magn. Magn. Mater.* **476** 142
[27] Zhai X B, Wang Y G, Zhu L, Zheng H, Dai Y D, Chen J K and Pan F M 2019 *J. Magn. Magn. Mater.* **480** 47
[28] Fan X D, Zhang T, Yang W M, Luan J H, Jiao Z B and Li H 2023 *J. Mater. Sci. Technol.* **147** 124
[29] Hou L, Jiang C, Liu H, Luo Q, Fan X D, Li W H and Li M R 2021 *J. Alloys Compd.* **859** 157863
[30] Fan X D, Zhang T, Jiang M F, Yang W M and Shen B L 2019 *J. Non-Cryst. Solids* **503–504** 36
[31] Jia X J, Zhang W, Dong Y Q, Li J W, He A N, Luan J H and Li R W 2022 *J. Alloys Compd.* **920** 166030
[32] Herzer G 1989 *IEEE Trans. Magn.* **25** 3327
[33] Ohta M and Yoshizawa Y 2007 *Appl. Phys. Lett.* **91** 062517
[34] Meng Y, Pang S J, Chang C T, Bai X Y and Zhang T 2021 *J. Magn. Magn. Mater.* **523** 167583
[35] Han Y, Inoue A, Kong F L, Chang C T and Al-Marzouki F 2016 *J. Alloys Compd.* **657** 237
[36] Herzer G 2013 *Acta Mater.* **61** 718
[37] Zhang H, Wang Z, Wen Z P and Wang J 2014 *IEEE Trans. Magn.* **50** 7
[38] Kulik T, Matyja H and Lisowski B 1984 *J. Magn. Magn. Mater.* **43** 135
[39] Suzuki K, Ito N, Garitaonandia J S, Cashion J D and Herzer G 2008 *J. Non. Cryst. Solids* **354** 5089
[40] Hono K, Ping D H, Ohnuma M and Onodera H 1999 *Acta Mater.* **47** 997
[41] Castellero A, Moser B, Uhlenhaut D I, Torre F H D and Löffler J F 2008 *Acta Mater.* **56** 3777
[42] Lv Z.W, Yuan C C, Ke H B and Shen B L 2021 *J. Mater. Sci. Technol.* **69** 42
[43] Ke H B, Zhang P, Sun B A, Zhang P G, Liu T W, Chen P H, Wu M and Huang H G 2019 *J. Alloys Compd.* **788** 391
[44] Li W, Zuo X F, Liu R, Pang C M, Jin F, Zhu W W and Yuan C C 2024 *Int. J. Plast.* **174** 103893
[45] Hou L, Shen P F, Wang B J, Shang Q Z, Liu L, Huang Y, Feng H C, Sun J, Liu H S and Li W H 2023 *Mater. Today Commun.* **35** 106012
[46] Chang C, Zhang H P, Zhao R, Li F C, Luo P, Li M Z and Bai H Y 2022 *Nat. Mater.* **21** 1240
[47] Wang Q, Liu J J, Ye Y F, Liu T T, Wang S, Liu C T, Lu J and Yang Y 2017 *Mater. Today* **20** 293
[48] Qiao J C, Wang Q, Pelletier J M, Kato H, Casalini R, Crespo D, Pineda E, Yao Y and Yang Y 2019 *Prog. Mater. Sci.* **104** 250
[49] Takeuchi A and Inoue A 2005 *Mater. Trans.* **46** 2817
[50] Zhao C.L, Wang A D, He A N, Yue S Q, Chang C T, Wang X M and Li R W 2016 *J. Alloys Compd.* **659** 193
[51] Pang J, Wang A D, Yue S Q, Kong F Y, Qiu K Q, Chang C T, Wang X M and Liu C T 2017 *J. Magn. Magn. Mater.* **433** 35
[52] Meng Y, Pang S J, Chang C T, Luan J H, Inoue A and Zhang T 2023 *J. Alloys Compd.* **940** 168799
[53] Milkova D A, Bazlov A I, Zanaeva E N, Churyumov A Y, Strochko I V, Ubyivovk E V and Inoue A 2023 *J. Non-Cryst. Solids* **609** 122234
[54] Kong F L, Chang C T, Inoue A, Shalaan E and Al-Marzouki F 2014 *J. Alloys Compd.* **615** 163
[55] Makino A, Kubota T, Makabe M, Chang C T and Inoue A 2008 *Mater. Sci. Eng. B* **148** 166
[56] Xu J, Yang Y Z, Li W, Xie Z W and Chen X C 2017 *J. Alloys Compd.* **727** 610
[57] Wang A D, Zhao C L, He A N, Men H, Chang C T and Wang X M 2016 *J. Alloys Compd.* **656** 729
[58] Makino A, Men H, Kubota T, Yubuta K and Inoue A 2009 *J. Appl. Phys.* **105** 07A308
[59] Liu T, Li F C, Wang A D, Xie L, He Q F, Luan J H, He A N, Wang X M, Liu C T and Yang Y 2019 *J. Alloys Compd.* **776** 606